Simulations of the premelting of Al(110)

Stoltze, Per

Published in:
Journal of Chemical Physics

Link to article, DOI:
10.1063/1.458308

Publication date:
1990

Document Version
Publisher's PDF, also known as Version of record

Simulations of the premelting of Al(110)

Per Stoltze
Laboratory of Applied Physics, Building 307, Technical University of Denmark, DK-2800 Lyngby, Denmark

(Received 21 July 1989; accepted 1 February 1990)

The premelting of Al(110) is studied by molecular dynamics simulations using the potential for Al derived from effective medium theory. We find a progressive disordering of the surface region as the bulk melting point is approached. This disorder is mediated by the formation of adatom–vacancy pairs. Based on the calculated radial distribution function and the analytical expression for the energy, it is demonstrated that the thermodynamics of disorder and melting is reflected in the single particle properties by a decrease in the number of nearest neighbors. The Debye temperature for the surface layer as determined from the simulations is $\theta_D \sim 250$ K, compared to $\theta_D \sim 320$ K found for the deeper layers. The thickness of the surface region determined from the Debye temperature is 3–4 layers. From an examination of the properties of some order parameters, we find that the premelting appears anisotropic only for some choices of order parameter. This has implications for the *detection* of the disorder by a diffraction technique.

Although all metallic elements form a liquid in some part of their phase diagram,[1] a number of other problems related to the melting of metals remain. Among these are the dynamics of the bulk melting process[2,3] and the structure of the crystal-melt interface.[4,5] The understanding of the structure of the surface of the hot crystal is related to the problem of the melting of metals by the hypothesis by Tammann (1910) that surfaces play an important role as sources of defects in the bulk melting process. While the melting process for bulk metals is a first-order phase transition, the presence of the surface reduces the symmetry and the order of the transition at the surface may differ from that of the bulk and the surfaces of metals may show *premelting*, defined as a progressive disordering of the surface of the metal as the melting point for the bulk is approached.

The premelting phenomenon has recently been studied intensively under ultrahigh-vacuum conditions by ion scattering,[6–11] LEED[12–14] and x-ray diffraction.[15] For the open Pb(110) surface premelting has been detected at temperatures much below the bulk melting point.[7] The premelting of this surface is suppressed by the chemisorption of oxygen. The close-packed Pb(111) surface does not show premelting,[9] the disorder on this surface is limited to less than one monolayer even at temperatures close to the bulk melting point. Contrary to the Pb(110) and Al(110) surfaces, the Al(100)[16] and Ni(110)[17] do not show premelting.

The nature of the transition at surfaces at the bulk melting point has been investigated in a continuum model.[18–22] In this model the atomic arrangement is replaced by an order parameter field and the atomic bonds are replaced by a coupling strength for the order parameter field. If we discard the possibility of the surface being more ordered than the bulk, two cases remain. In the first case, the coupling strength at the surface is about the same as in the bulk. The order at the surface is lower than in the bulk, but the order parameter jumps from a nonzero value to zero at the bulk melting point. The surface undergoes a first-order transition at the bulk melting point, but the latent heat of melting for the surface may be different from the bulk. In the second case, the order parameter in the surface is lower than in the bulk and goes continuously to zero at the bulk melting point. The surface undergoes a second-order phase transition. In this case the surface premelting is a reflection of the continuous nature of the phase transition at the surface.

The premelting phenomenon has been treated in a model based on the interface thermodynamics.[10] In this model the premelting occurs when the quasiliquid layer formed below the melting point wets the surface of the hot crystal. This model successfully rationalizes the observation of premelting for Pb(110), the absence of premelting for Pb(111), and Ni(110) and the suppression of premelting by chemisorbed atoms.

The description of the disorder at the level of atomic structure is beyond the description of the disorder by an order parameter field, as well as the description by macroscopic thermodynamics.[23]

One reason for studying the properties of hot metal surfaces by computer simulation is that computer simulations bridge experiments and theory. While theories of atomic interactions may give detailed and accurate descriptions of the energy of the system, the properties at finite temperature are determined by the free energy rather than the energy. Computer simulations may be viewed as one way of determining the entropy of the potential. When the understanding of the atomic properties have been developed to the limit of agreement with experiments, interesting information may be derived by systematic calculations. These calculations may aid in the interpretation of experiments and may even supply data for physical quantities for which no experimental technique exists.

The premelting of crystals has been studied by computer simulation using molecular dynamics and Lennard-Jones potentials. For fcc crystals, premelting has been found for the (100), (110), and (111) surfaces.[24–26] The premelting is

 0021-9606/90/106306-16$03.00

mediated by adatoms–vacancy pairs.[27] The important role of surface phonons in the simulations and the differences between roughening and premelting have been studied.[28] Recently, the behavior of Ni(110) at high temperature has been studied by computer simulation[17] using a potential derived by the embedded atom method. These simulations show that this surface does not show premelting. This observation is in agreement with thermodynamic considerations.[10]

In this paper we report the results of one series of simulations of the premelting of Al(110) using a potential derived from the effective medium theory. In preliminary notes we have reported on the application of this potential in simulations of Al surfaces. We have found that Al(110) shows premelting while Al(111) does not[29] and that the answer to the question of whether the surface premelting isotropic may depend on the details of the comparison of the structure factors.[30]

I. EFFECTIVE MEDIUM THEORY

It is tempting to try to represent the interaction energy for a system of atoms as a sum of pairwise interaction energies. Although the Coulomb interaction to be put into the Schrödinger equation do have this form, the resulting interaction energies for the *atoms* may have a more complicated form. For metals the delocalization of valence electrons causes the presence of a volume dependent term in the total energy for the metal and a single pair potential will not be able to reproduce the cohesive energy, the bulk modulus and the surface energy for a metal.

The potential used in the following is based on effective medium theory. This model is based on a small number of well defined approximations.[31,32] I shall not try to give any detailed exposition of this potential, rather I will try to expose details important for the use of effective medium theory in simulations of simple metals.

Effective medium theory is based on the idea that due to the existence of a variational principle for the electron density we may be able to get away with using quite simple trial electron densities. The trial densities used are superpositions of atom-like densities. The atoms are represented as neutral, possibly overlapping spheres. For the simulations, the use of *neutral* spheres is particularly attractive as the Madelung term will be identically zero.

All parameters in effective medium theory may be determined from calculations without reference to experiments. This procedure would avoid the complexity that might result if the parameters were obtained by an *a priori* interpretation of the same experimental data that one ultimately wants to investigate by simulations. However, the calculation of all parameters in the potential may not be preferable for simulations. In brief,[32] the presence of Fridel oscillations in the calculations of the parameters causes a slight arbitrariness in the elastic constants determined from the potential. One solution[32] to this problem is to choose from the range of calculated parameters, the set of data most closely reproducing the experimental C_{44}. By construction the effective medium theory gives a good and computationally effective approximation to the description of metallic systems. Effective medium theory, in its more recent formulation,[31] has been applied to the description of bulk[31–33] and surface[31–34] properties of metals, to reconstruction[35,36] and surface melting,[29,30] to chemisorption dynamics[37] and to hydrogen in metals.[38]

For simple metals such as Al there are no open d shells and the potential energy of the system is [Ref. 31, Eq. (7.21)]

$$E=\sum_i E_c(i)+\Delta E_{\rm AS}(i), \tag{1}$$

where the summation runs over all atoms in the ensemble.

E_c depends on the density of the system. It may be expanded as a series [Ref. 31, Eq. (7.22)]

$$E_c(i)=E_0+E_2\left(\frac{\bar n(i)}{n_0}-1\right)^2+E_3\left(\frac{\bar n(i)}{n_0}-1\right)^3, \tag{2}$$

where n_0 is the equilibrium electron density. The Wigner–Seitz sphere of an atom is defined as the neutral sphere centered in the nucleus of the atom. The averaged density $\bar n$ induced by the neighbors in the Wigner–Seitz sphere of atom number i is [Ref. 31, Eqs. (7.18), (7.19), (C1) and (C8)]

$$\bar n=n_0\exp(\eta s_0)\left(\frac{\sigma_1(i)}{12\gamma_1}\right)^{\eta/\beta\eta_2} \tag{3}$$

$$\sigma_1(i)=\sum_{j\neq i}\exp(-\eta_2 r_{ij})\theta(r_{ij}), \tag{4}$$

where we have used the shorthand notation

$$\mathbf{r}_{ij}=\mathbf{r}(i)-\mathbf{r}(j), \tag{5}$$

$$\mathbf{r}_{ji}=-\mathbf{r}_{ij}, \tag{6}$$

$$r_{ij}=|\mathbf{r}_{ij}|. \tag{7}$$

In these equations η and η_2 are inverse screening lengths, γ_1 is a normalization allowing for the extension of the summation in Eq. (4) to include remote neighbor pairs and β is a constant of geometric origin,

$$\beta=\left(\frac{16\pi}{3}\right)^{1/3}\left(\frac{1}{2}\right)^{1/2}, \tag{8}$$

$\theta(r)$ is a step function. For this we have used

$$\theta(r)=\{1+\exp[a(r_c-r)]\}^{-1}, \tag{9}$$

where r_c is the cutoff radius and a determines the steepness of the cutoff.

The use of Wigner–Seitz *spheres* will cause parts of space to be inside two spheres while other parts of space are not inside any sphere. This generates an electrostatic energy term [Ref. 31, Eq. (7.14)]:

$$\Delta E_{\rm AS}=\alpha(\bar n-n_{\rm fcc}), \tag{10}$$

where α is a parameter of the potential. This term is calculated using a perfect fcc lattice with the same $\bar n$ as a reference state [Ref. 31, Eqs. (7.20) and (C9)]:

$$n_{\rm fcc}=n_0\exp(\eta s_0)\frac{\sigma_2(i)}{12\gamma_2}, \tag{11}$$

$$\sigma_2(i)=\sum_{i\neq j}\exp\left(-\frac{\eta}{\beta}r_{ij}\right)\theta(r_{ij}). \tag{12}$$

In this equation, γ_2 is a normalization allowing for the extension of the sum to remote neighbor pairs.

TABLE I. A listing of the number of neighbors and their distance from the central atom in a perfect lattice. From this information the cutoff radius, r_c, in Eq. (9) may be determined for Al from the number of shells to be included in the calculation of forces and energy. For each choice of cutoff radius, the values of γ_1 and γ_2 have been calculated from Eq. (13).

Shell	Neighbors	Distance	r_c	γ_1	γ_2
1	12	βs_0	6.55	1.000	1.000
2	6	$\sqrt{2}\beta s_0$	8.34	1.029	1.042
3	24	$\sqrt{3}\beta s_0$	10.13	1.042	1.066
4	12	$2\beta s_0$	11.50	1.043	1.069
5	24	$\sqrt{5}\beta s_0$	12.71	1.043	1.070

Throughout this study we will assume that γ_1 and γ_2 are functions of the cutoff only. They are introduced to allow the inclusion of contributions to the density beyond nearest neighbors. In a perfect fcc structure at optimum lattice constant, $\bar{n} = n_0$ and $n_{\rm fcc} = n_0$. This defines γ_1 and γ_2 in terms of the cutoff used [Ref. 31, Eqs. (C6) and (C10)].

$$\left.\begin{aligned}\sigma_1 &= 12\gamma_1\\ \sigma_2 &= 12\gamma_2\end{aligned}\right\} \quad \text{for optimum fcc,} \tag{13}$$

where the summations in Eqs. (4) and (12) extend over a perfect fcc lattice at the optimum lattice constant. A number of consistent values of r_c, γ_1, and γ_2 are listed in Table I. The complete set of parameters used is listed in Table II.

A number of features in the potential will be immediately apparent in the output from simulations. E_c is minimal for $\bar{n} = n_0$, Eq. (2). This density determines the optimum lattice constant at low temperature and the corresponding energy, $E_c = E_0$, is the cohesive energy. The curvature of E_c at the minimum determines the bulk modulus (Sec. C of Ref. 31). The differences in energy between different crystal structures (SC, bcc, fcc) are determined by $E_{\rm AS}$. The major contribution to the energy of phonons will come from $\Delta E_{\rm AS}$ (Sec. D of Ref. 31).

At finite temperature the major contribution to C_p will come from $\Delta E_{\rm AS}$ rather than from E_c. This observation from the simulations may be explained qualitatively by the following brief argument. The properties of the system at finite temperature are determined by the *free* energy, $\Delta F = \Delta U - T\Delta S$. Since E_c is determined by the density of the system (i.e., the lattice constant), while $\Delta E_{\rm AS}$ is determined by the relative positions of all atoms, the entropy S, of the latter term will be the largest. The thermal energy at not-too-high temperatures will be close to the Dulong and Petit value of $3k_BT$. The larger entropy of the atomic sphere term causes approximately 95% of the potential energy to be absorbed by $\Delta E_{\rm AS}$.

For a surface at high as well as at low temperature, E_c and $\Delta E_{\rm AS}$ give comparable contributions to the surface energy (Sec. E of Ref. 31). The outermost layers have $\bar{n} < n_0$, due to the missing neighbors. At low temperatures the first layer relaxes inward increasing $\bar{n}$, this distortion of the lattice increases $\Delta E_{\rm AS}$ for both the first and second layer. The exact magnitude of the relaxation is found when the inward force is balanced by the outward force.

The force acting on atom number i is

$$\mathbf{F}(i) = -\frac{\partial E}{\partial \mathbf{r}(i)} \tag{14}$$

$$= \frac{\partial E(i)}{\partial \bar{n}(i)}\frac{\partial \bar{n}(i)}{\partial \sigma_1(i)}\frac{\partial \sigma_1(i)}{\partial \mathbf{r}(i)} + \frac{\partial E(i)}{\partial n_{\rm fcc}(i)} \times \frac{\partial n_{\rm fcc}(i)}{\partial \sigma_2(i)}\frac{\partial \sigma_2(i)}{\partial \mathbf{r}(i)} + \sum_j \frac{\partial E(j)}{\partial \bar{n}(j)}\frac{\partial \bar{n}(j)}{\partial \sigma_1(j)}\frac{\partial \sigma_1(j)}{\partial \mathbf{r}(i)} + \sum_j \frac{\partial E(j)}{\partial n_{\rm fcc}(j)}\frac{\partial n_{\rm fcc}(j)}{\partial \sigma_2(j)}\frac{\partial \sigma_2(j)}{\partial \mathbf{r}(i)}, \tag{15}$$

where

$$\frac{\partial E(i)}{\partial \bar{n}(i)} = \frac{2E_2}{n_0}\left[\frac{\bar{n}(i)}{n_0} - 1\right] + \frac{3E_3}{n_0}\left[\frac{\bar{n}(i)}{n_0} - 1\right]^2 + \alpha, \tag{16}$$

$$\frac{\partial E(i)}{\partial n_{\rm fcc}} = -\alpha, \tag{17}$$

$$\frac{\partial \bar{n}(i)}{\partial \sigma_1(i)} = \frac{\eta \bar{n}}{\beta \eta_2 \sigma_1(i)}, \tag{18}$$

$$\frac{\partial n_{\rm fcc}(i)}{\partial \sigma_2(i)} = \frac{n_{\rm fcc}}{\sigma_2(i)}, \tag{19}$$

$$\frac{\partial \sigma_1(i)}{\partial \mathbf{r}(i)} = \sum_j \exp(-\eta_2 r_{ij})\left[\frac{\partial \theta(r_{ij})}{\partial r_{ij}} - \eta_2 \theta(r_{ij})\right]\frac{\mathbf{r}_{ij}}{r_{ij}}, \tag{20}$$

$$\frac{\partial \sigma_1(j)}{\partial \mathbf{r}(i)} = \exp(-\eta_2 r_{ij})\left[\frac{\partial \theta(r_{ij})}{\partial r_{ij}} - \eta_2 \theta(r_{ij})\right]\frac{\mathbf{r}_{ij}}{r_{ij}}, \tag{21}$$

$$\frac{\partial \sigma_2(i)}{\partial \mathbf{r}(i)} = \sum_j \exp\left(-\frac{\eta}{\beta} r_{ij}\right)\left[\frac{\partial \theta(r_{ij})}{\partial r_{ij}} - \frac{\eta}{\beta}\theta(r_{ij})\right]\frac{\mathbf{r}_{ij}}{r_{ij}}, \tag{22}$$

$$\frac{\partial \sigma_2(j)}{\partial \mathbf{r}(i)} = \exp\left(-\frac{\eta}{\beta} r_{ij}\right)\left[\frac{\partial \theta(r_{ij})}{\partial r_{ij}} - \frac{\eta}{\beta}\theta(r_{ij})\right]\frac{\mathbf{r}_{ij}}{r_{ij}}. \tag{23}$$

For molecular dynamics simulations the force calculation is necessary. The energy calculation may in principle be spared but the energy is often calculated to check the energy conservation continuously during the calculation. Computations using the effective medium theory potential are more demanding than computations using a pair potential. However, using an interaction list with the minimum image convention,[39] the size of the computation can be brought to scale as N (rather than N^2), where N is the number of atoms in the ensemble. Further, each of the terms

$$\exp(-\eta r_{ij}),$$

and

$$\exp\left(-\frac{\eta_2}{\beta} r_{ij}\right)$$

will occur twice in the energy calculation and six times in the force calculation. This may be used to reduce the computational effort substantially. For molecular dynamics it is possible to shift the hot spot of the program away from the exp and sqrt functions. The resulting gain in speed compared to a naive N^2 algorithm is about 100 times for $N = 500$ atoms and about 1200 times for $N = 2000$ atoms.

The algorithm sketched above is much more efficient than the algorithm we have used earlier.[33] We may perform a molecular dynamics simulation using 512 atoms and 15 000 time steps in 8 h on a 10 MFLOP (single precision) computer. Even if the computational effort in simulations

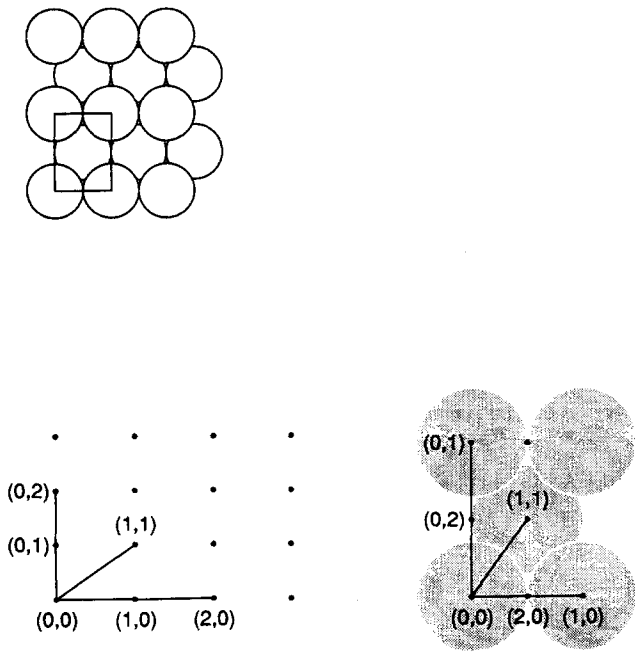

FIG. 1. The upper diagram illustrates the conventional unit cell for a fcc (110) surface. We have oriented the close-packed {110} rows from the bulk unit cell along the x axis of the surface unit cell. The lower figure shows the (1,0), (0,1), (2,0), (1,1), and (0,2) wave vectors drawn in the reciprocal space (left) and the inverse of these vectors drawn in real space (right).

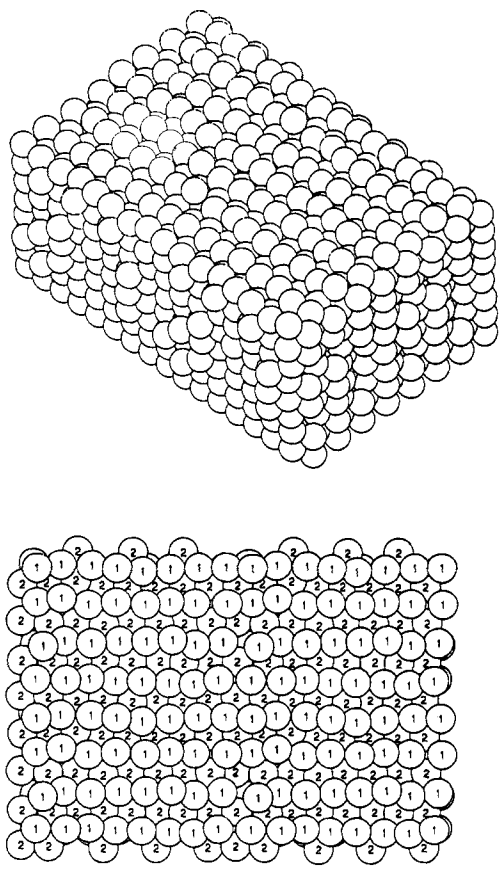

FIG. 2. Snapshot and projection of the Al(110) surface at 560 K. In the snapshot the system has been replicated in the X and Y direction in the production of the figure. In the projection the atoms have been labeled by layer number. At this temperature the surface is only slightly disordered and the presence of the close-packed rows is obvious.

using the effective medium theory potential is larger than for pair potentials, the computational effort is moderate.

II. SIMULATIONS

In this study of Al(110) we have used a setup of 512 atoms distributed in 16 layers with 32 atoms per layer. Periodic boundary conditions are used in X and Y. The conventional surface unit cell is shown in Fig. 1 in both direct and reciprocal space. Since the simulations are made in the direct space, Fig. 1 also shows, drawn in the inverse lattice, the wave vectors used in the calculation of structure factors as well as the inverse of those wave vectors drawn in the direct space. Snapshots of the system at high temperature are shown in Figs. 2, 3, and 4.

Layers are numbered from the surface. The outermost layer when all atoms are at their perfect lattice position is layer number 1. The atoms of the four lowest layers are kept at their perfect lattice positions. The number of static layers has been chosen so that the interaction energy between any dynamic atom and the static surface will be zero. This means that we are essentially simulating a semiinfinite crystal rather than a slab. The lattice constant for the static substrate equals the equilibrium lattice constant at the actual temperature. The equilibrium lattice constant has been determined by Monte Carlo simulations for the bulk crystal.

The static substrate eliminates the problems caused by the presence of two free surfaces, such as spontaneous rota-

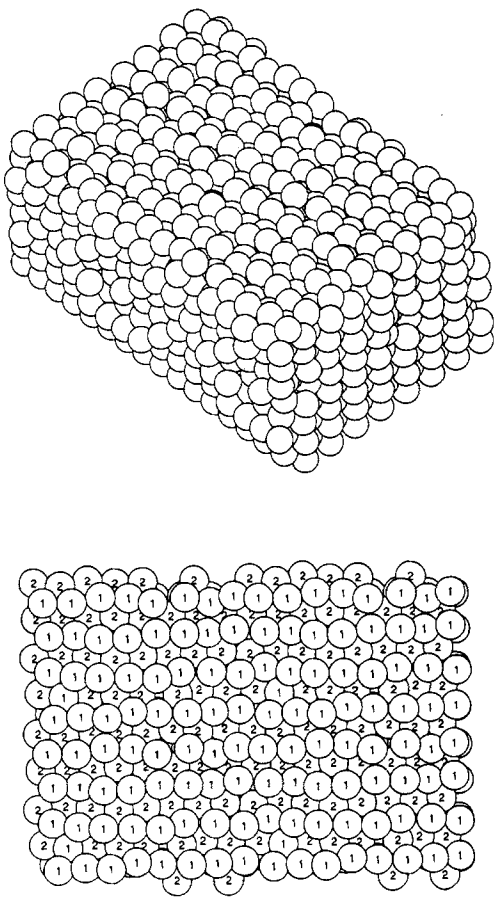

FIG. 3. Snapshot and projection of the Al(110) surface at 745 K.

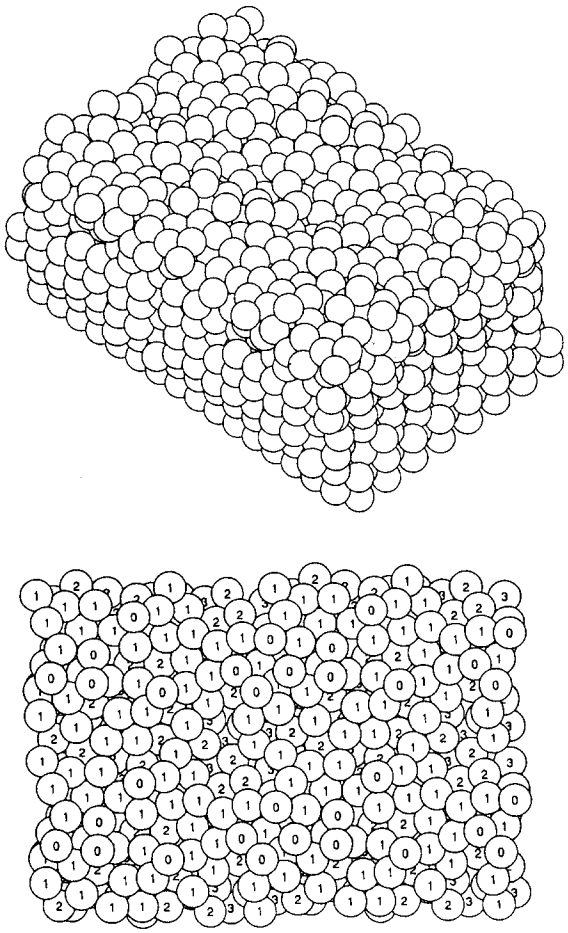

FIG. 4. Snapshot and projection of the Al(110) surface at 930 K. At this temperature the surface is more disordered and several adatom–vacancy pairs can be found.

tion to expose a more stable surface. Associated with the surface covered by the static atoms (i e., the underside of the system as drawn in Figs. 2, 3, and 4) there will be an energy ΔE. For some property $A(\mathbf{r},\mathbf{p})$ the canonical equilibrium average $\langle A \rangle$ is given by

$$\langle A \rangle = Z^{-1} \int A(\mathbf{r},\mathbf{p}) e^{\beta(E+\Delta E)}\, d\mathbf{r}\, d\mathbf{p}, \tag{24}$$

$$Z = \int e^{\beta(E+\Delta E)}\, d\mathbf{r}\, d\mathbf{p}, \tag{25}$$

ΔE will cancel out of the average $\langle A \rangle$ and the average will be unaffected by the presence of the static surface. From this argument it is immediately apparent that the results obtained for the outermost layers are independent of the presence of the static substrate. This argument will of course not be valid if the static atoms directly affects $A(\mathbf{r},\mathbf{p})$ in the above equation.

The atoms in the static layers having no kinetic energy form a perfect thermal insulator. The atoms in the lower dynamic layers will not lose energy by interaction with the static atoms, but the static atoms have an artificially high order. This will cause a problem when the number of disordered layers becomes comparable to the number of dynamic layers. The direct interaction between disordered layers and the static atoms will cause the disordered atoms in close contact with the static substrate to have properties quite different from the bulk liquid.

The simulations were done using molecular dynamics. The integration of the classical equations of motion was performed using the velocity-Verlet algorithm.[39] The elementary time step in the algorithm was 1.2 fs. The conservation of energy by the program during microcanonical simulations was 1 meV/atom or better over 5000 steps.

At the start of the simulations, the atoms were placed at their perfect lattice positions and their momenta drawn from a Maxwell–Boltzmann distribution. The system was then propagated through 6 ps with stochastic temperature control.[39] The thermalization was then stopped and the system was allowed to evolve microcanonically for 3 ps while thermodynamic averages are collected. In the calculation of averages one would like to reduce the continuous observation of the system to a smaller number of independent observations. We introduce the approximation that snapshots separated by a time interval at least as long as the period of the cosine component of the momentum autocorrelation, $\langle \mathbf{p}(0)\cdot\mathbf{p}(t) \rangle$, may be treated as statistically independent observations of the system.

Periods of thermalization were used between periods of averaging. Propagation of the system by microcanonical molecular dynamics during the collection of snapshots reduces the number of snapshots necessary for the calculation of reliable averages. However, the periods of thermalization are important, primarily because they are the only means of supplying the latent heat of melting. Second, since a limited number of atoms are used in the simulations it may be possible to construct a setup where the system runs on a small cycle, rather than exploring phase space. It is unlikely that this problem could persist through periods with stochastic temperature control.

The simulations were propagated at least until averages collected over 3 ps periods separated by thermalization remained constant. For temperatures close to the melting point this required that the system was followed for more than 60 ps. Temperatures much above or below the bulk melting point required less than half of this time. Besides the constant value for averages over 3 ps periods, we have verified that the averages of kinetic energy and the fluctuations in potential energy were in agreement with the values expected from the temperature and the number of particles.

Among the averages collected during the averaging are the energy, some structure factors, and the coordination number averaged for the system and for layers. For these data the slowest convergence is found for the structure factors for the deeper layers.

There are a number of implicit approximations in the treatment outlined above. As the de Broglie wavelength for Al is far shorter than the interatomic distances, the treatment of the atoms as classical particles instead of wave packets is a good approximation. A second approximation concerns the treatment of the electron gas. In most potentials it is an implicit assumption that the electron gas will remain in its ground state. Presumably this will only cause a problem for thermodynamic calculations at temperatures far higher

than considered here. A third approximation concerns the use of classical mechanics. At low temperatures the classical mechanics will give a wrong treatment of phenomena related to the quantization of energy. The lower limit of validity for the classical treatment is determined by the required precision and depends on the phenomenon under consideration, the limit is approximately equal to the Debye temperature. However, classical simulations below the Debye temperature are not meaningless as the deviations from the quantum mechanical description are well known.

During the collection of averages the system evolves microcanonically, i.e., at constant total energy. Since the number of particles is limited, the kinetic energy will fluctuate. One interpretation is that the temperature undergoes fluctuations. Another interpretation is that the temperature is well defined and constant but that the fluctuations constitute a limitation to the determination of the temperature. The conclusion is that, in simulations using a small number of particles in a thermally insulated system, the concept of temperature must be treated with some caution.

A major problem in the computation of thermodynamic data by simulations are the finite size effects. The use of a small number of atoms will cause differences in the data compared to the limit of an infinite number of particles. For a first-order transition the finite size effects will cause some rounding of the transition,[40] the rounding is not expected to be large enough to cause a confusion between first- and second-order transitions for the situation considered here. To check for possible problems we have performed some calculations for a system of twice the linear dimension in x and y (i.e., 2048 atoms rather than 512 atoms distributed in 12 dynamic and 4 static layers). The obtained results agree with those presented below except that the onset of the disorder for the larger system appears more smooth. This will be discussed in detail below.

III. LAYER STRUCTURE

At higher temperatures atoms will start to move through the system by diffusion and by the time the thermalization is completed, an atom may be found quite far from its original lattice position. As an error in the assignment of layer number for an atom can cause a substantial error in the calculated structure factor for a layer, we have chosen to reassign layer numbers for all atoms in the analysis of each snapshot. The problem of performing a *fast* assignment of the layer number may be solved by comparing the identification of the layers to the problem of making a best fit of a train of delta functions

$$\sum_n \delta(z - nd - d_0) \tag{26}$$

to the density profile. In this equation d is the interlayer spacing, n is the layer number and d_0 is the z coordinate for layer number zero. At zero temperature and with suitable bounds on n this train of delta functions is the density profile $\rho(z)$. The idea behind the algorithm is that the Fourier

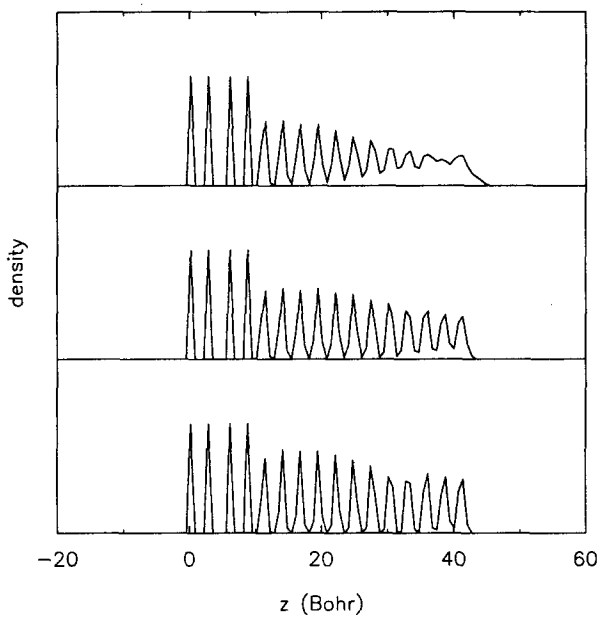

FIG. 5. Average density in arbitrary units projected on the z axis at 560 (lower), 745, and 930 K (upper). Figures 2–4 show typical snapshots of the surface at these temperatures.

TABLE II. Parameters used in the simulations. The cutoff in the energy calculation corresponds to the inclusion of first and second shell. (1 bohr = 0.52 Å).

Parameter	Value	Unit	
n_0	0.007	bohr^{-3}	Eqs. (3) and (11)
s_0	3.000	bohr	Eqs. (3) and (11)
η	2.000	bohr^{-1}	Eqs. (3), (11), and (12)
η_2	1.270	bohr^{-1}	Eq. (3)
α	1280.	eV/bohr^{-3}	Eq. (10)
E_0	−3.28	eV	Eq. (2)
E_2	1.12	eV	Eq. (2)
E_3	−0.35	eV	Eq. (2)
γ_1	1.0210	(dimensionless)	Eqs. (3) and (13), Table I
γ_2	1.042	(dimensionless)	Eqs. (11) and (13), Table I
r_c	8.54	bohr	Eq. (4), (9), and (12)
r_{cn}	6.55	bohr	Eq. (31)
β	1.809	(dimensionless)	Eq. (3), (12)

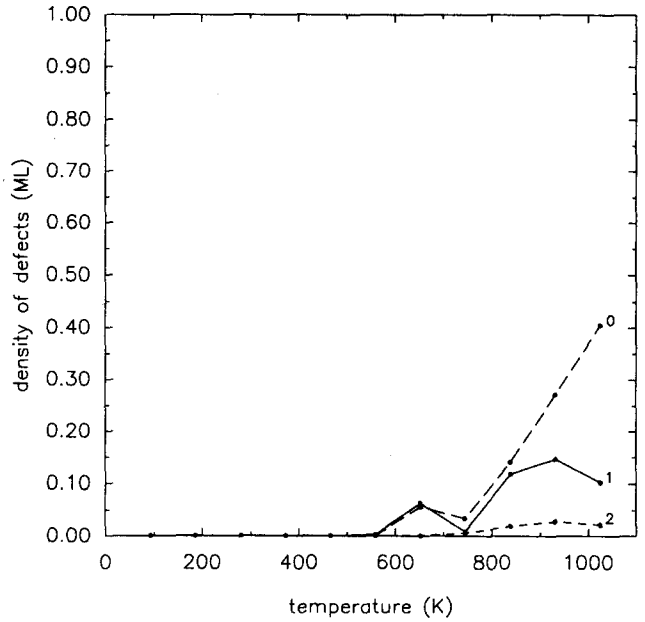

FIG. 6. Density of defects (in monolayers) as a function of temperature as measured by x_l. The presence of vacancies in layers 1 and 2 and adatoms in layer number 0 is obvious. As discussed in the text, it is less obvious from this way of presenting the data, that the details of the simulation force the creation of adatoms and vacancies in pairs.

transform of the train of delta functions will remain the dominating term in the Fourier transform of $\rho(z)$ at higher temperatures. For a system of a limited number of layers we may assume that d is the interlayer spacing for the perfect lattice. The value of d_0 may then be determined from a Fourier transform of the density profile and the layer number for each atom calculated from the values of d and d_0. This algorithm will fail in the case the system does not have a layered structure or if excessive vibration causes large variations in the interlayer spacing. Examination of the Fourier coefficients will reveal this failure.

Figure 5 shows the averaged density projected on the z axis at 560, 745, and 930 K. At the lower temperature the layer structure may easily be identified while at the higher temperatures the premelting of the surface results in a partial dissolution of the layer structure. The presence of adatoms is noticeable by the slow decay of the density at the surface at high temperatures.

IV. DEFECTS IN LAYERS

The analysis of the properties of layers becomes difficult for layers near the surface at higher temperatures, simply because the premelting makes the concept of *layers* ambiguous. For temperatures low enough to make a separation into layers meaningful, we may define a density of defects, x_l as

$$x_l = \begin{cases} \dfrac{n_0 - \langle n \rangle}{n_0} & \text{for } l \geqslant 1 \\ \dfrac{\langle n \rangle}{n_0} & \text{for } l < 1 \end{cases} . \tag{27}$$

In words, x_l measures the number of atoms missing from a layer below the position of the ideal surface and the number of atoms in a layer above the ideal surface. Figure 6 shows x_l as a function of temperature. It is obvious that at higher temperatures atoms move from the surface to a layer of adatoms.

In layer number 1 the enthalpy of formation for a vacancy, as determined from an Arrhenius plot of $x_l(T)$, is 340 meV; the entropy, is positive 1.8 k_B. In layers number 2 to 4 the enthalpy is 260–290 meV; the entropy is negative, -0.5 to $-1.0\ k_B$. Below the fourth layer the number of missing atoms is statistically insignificant. For adatoms this analysis gives an enthalpy of formation of 480 meV; the entropy is 4.5 k_B.

These data illustrate a problem in the interpretation of the thermodynamic data for defects. The definition of x_l is intuitively a reasonable measure of the concentration of defects and the calculated enthalpies of formation are reasonably close to the calculated enthalpy of 0.30 eV for the transfer of an atom from the Al(110) surface to the layer of adatoms. However, the enthalpy of formation calculated from x_l is not really a well defined thermodynamic quantity. We know from the way the simulations have been done that, when an atom has moved up to create a vacancy below the surface, the atom will be found above the surface. By using x_l as a measure of the concentration of defects, we ignore that these defects must be created in pairs.

V. ENERGY OF LAYERS

Figure 7 shows the thermally averaged energy for layers number 1 through 10 as a function of temperature. At low temperature, the heat capacity of all layers is $3k_B$ as expected from the Dulong and Petit rule. Around 600 K the heat capacity of the first layer drops significantly below $3k_B$ and

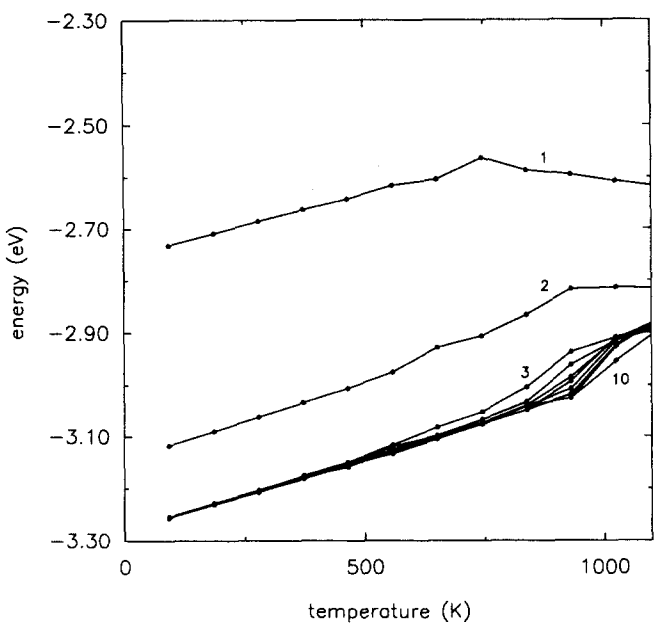

FIG. 7. Average total energy of layers number 1 through 10 as a function of temperature. Layers number 1 and 2 have a higher energy than the deeper layers and are stabilized by the formation of adatoms at higher temperature. For the deeper layers there is a sequential increase in energy around 950 K. It appears that the transition temperature increases with depth.

even becomes negative. The cause of the decrease in energy may be understood from the observation that the stabilization of layer number 1 coincides with the first observation of adatoms. These thermally formed defects stabilize layer number 1 by increasing the electron density for this layer.

Thermodynamic stability requires that the heat capacity of a closed system is positive. Although we may divide the system into layers based on the density profile, a layer is not a thermodynamically closed system since the number of atoms in each layer may vary with temperature.

At high temperatures there is an increase in the energy of the lower layers. This increase in energy coincides with a rapid decrease for the structure factor, this coincidence is the signature of a phase transition. The transition temperature is about 950 K for the outermost layers. It is obvious from Fig. 7, that the transition temperature increases with depth. The latent heat of the transition is about 100 meV. The agreement with the experimental melting point[41] at 933 K may be somewhat fortuitous. The presence of the static substrate makes the present simulations unsuited for an accurate determination of the bulk melting point. Based on other calculations we believe the melting point for the bulk may be up to $\sim 10\%$ higher than the experimental bulk melting point.

Before anything can be said if the surface transition is first or second order, the influence of finite size effects[3] must be examined in detail. However, the finite size effects will smooth the transition.[40] In the simulations the disorder is first detected much closer to the bulk melting point than the $\frac{2}{3}T_m$ expected from mean-field theory for a 2D layer[22] and, as the transition takes place over a limited temperature range, it is not inconceivable that the transition is first order.[42]

The Gibbs surface energy may be calculated as

$$U_s = \frac{\sum_i E_i - E_B}{n_0}, \tag{28}$$

where E_i is the actual energy of atom number i, E_B is the energy of an bulk atom at the same conditions, and n_0 is the ideal number of atoms in a layer. Contrary to the energy per layer, the surface energy is a well defined thermodynamic quantity. At low temperature the surface energy is caused by the loss for neighbors for the surface atoms with a small correction for relaxations and reconstructions. At higher temperatures additional contributions will come from the presence of surface defects, surface phase transitions and increased anharmonicity at the surface. Under these conditions several layers may contribute to the surface energy.

Figure 8 shows the calculated surface energy as a function of temperature. At low temperatures the surface energy is constant, approximately 650 meV. This equals the value calculated by hand from the potential at zero temperature. When the formation of surface defects sets in at higher temperature the surface energy increases steeply.

In this calculation it is an implicit assumption that we know the energy of the atom in the bulk. Since the bulk melting in simulations tends to show hysteresis due to the finite number of atoms and the periodic boundary conditions,[3] there will be a temperature range close to the bulk melting point where the energy of a bulk atom is a double valued function of temperature. For this reason the calculation of the surface energy should not be extended to temperatures too close to the bulk melting point. If defects are created in large numbers in the bulk it may be inappropriate to calculate the surface energy from a comparison of the *total* energies from an bulk and an semiinfinite crystal. By examination of the structure factors, the radial distribution function and real space pictures we do not find evidence for concentrations of bulk defects large enough to cause a problem for the calculation of the surface energy by comparison of total energies.

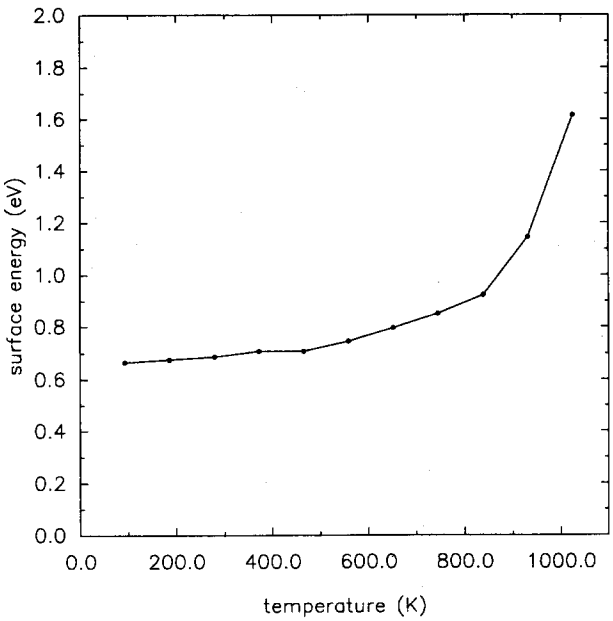

FIG. 8. Surface energy as a function of temperature (in K). The surface energy has been calculated as the difference between the actual energy of the system and the energy of the same number of bulk atoms. The ideal number of atoms in a layer is 32, this number has been used for normalization.

VI. THE RADIAL DISTRIBUTION FUNCTION

For temperatures low enough to make the concept of layers meaningful we may define a radial distribution function g_{xy} for the layer as

$$g_{xy}(r) = \langle \delta(r_{ij}) \delta(l_i - l_j) \rangle, \tag{29}$$

in analogy to the conventional pair correlation function, $g_2(r)$,

$$g_2(r) = \langle \delta(r_{ij}) \rangle. \tag{30}$$

For the bulk at low temperature, $g_2(r)$ has a peak at 5.22 bohr (nearest neighbor shell, 12 neighbors), 7.67 bohr (second shell, 6 neighbors) and 9.41 bohr (third shell, 24 neighbors). At higher temperatures the second and third shells merge into what appears to be one shell holding approximately 30 neighbors at 9.6 bohr.

Figure 9 shows the calculated $g_{xy}(r)$ for the surface layer at 560, 745, and 930 K. The $g_{xy}(r)$ is calculated by dividing the interval 0 through 15 bohr into a large number of

bins. The number of observations in each bin is counted during the simulations. Following the simulation the number of observations in the bins are examined and a running average is calculated. The window used in the averaging is chosen to give a reasonable signal-to-noise ratio for the calculated $g_{xy}(r)$.

In Fig. 9 the excluded volume inside the first shell[23] and the peaks due to the first and by the third shells are prominent. These peaks are found near their positions calculated for a hot bulk crystal. For g_{xy} there is no peak due to the second shell as next-nearest-neighbor pairs of atoms do not belong to the same layer for (110) surfaces in fcc. At higher temperatures distortions of the structure allow next-neighbor pairs to belong to the same layer, but at these temperatures the peaks due to the second and third shell merge.

Figure 10 shows the two-dimensional radial distribution function $g_{xy}(r)$ for layers number 1 through 10 for the crystal at 930 K. For layer number 10 $g_{xy}(r)$ strongly resembles the three-dimensional radial distribution function for a hot crystal. Intuitively one would not expect to see the next-nearest-neighbor peak close to 7.6 bohr in the two-dimensional radial distribution function. From real space pictures of snapshots from the deeper layers of the semiinfinite crystal, we find that the lattice generally looks like a distorted fcc lattice but briefly the local orientation of the lattice appears different from the (110) orientation of the system as a whole. Apparently these brief distortions are reflected in the two-dimensional radial distribution function.

Towards the surface there is a gradual transition of the appearance of $g_{xy}(r)$, and for the surface layer the only remaining features of $g_{xy}(r)$ are the excluded volume and the nearest-neighbor peak. The two-dimensional radial distribution function for the surface strongly resembles the three-dimensional radial distribution function for the bulk liquid. From the appearance of the surface, Fig. 4, this is hardly surprising.

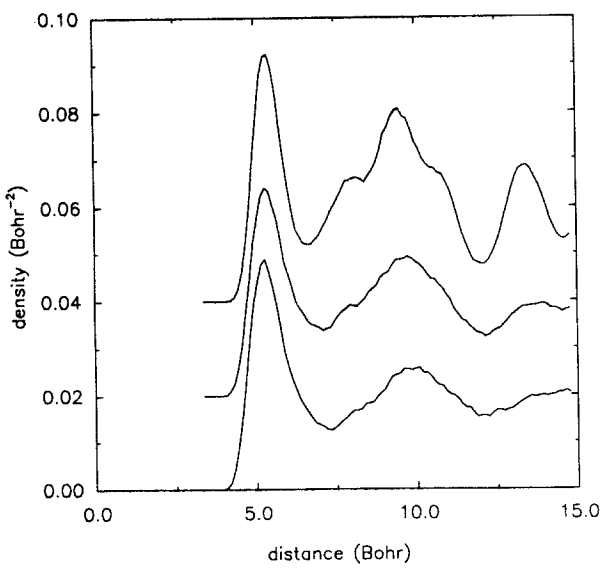

FIG. 9. The two-dimensional radial distribution function $g_{xy}(r)$ for layer number 1 at 560 (lower), 745, and 930 K (upper). The radial distribution function is in units of bohr^{-2}, the interatomic distance in units of bohr, 1 bohr = 0.52 Å. The figures have been displaced vertically to avoid overlap.

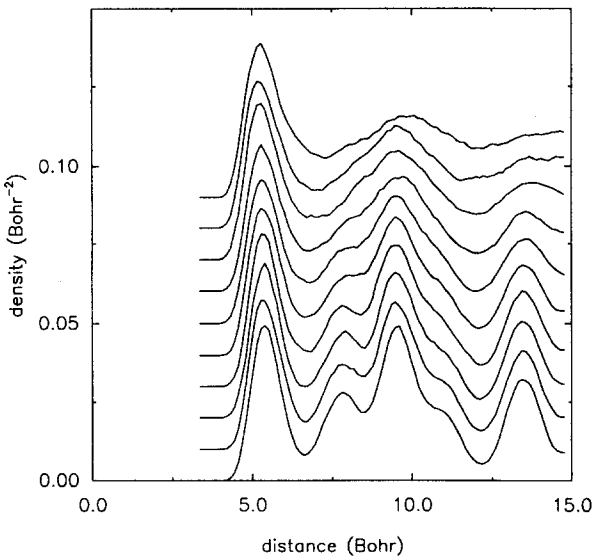

FIG. 10. The two-dimensional radial distribution function $g_{xy}(r)$ for layers number 1 (upper) through 10 (lower) at 930 K. This figure is directly comparable to Fig. 9.

In a previous paper[29] we truncated the potential between the first and second shell. While this is no consequence for the properties at low temperatures, and of little importance for some high-temperature properties, such as the energy, the heat capacity, and the thermal expansion, we have found that the bulk melting point is sensitive to the details of the choice of $\theta(r)$. For this reason we prefer to extend the potential beyond the nearest-neighbor shell. The effect of truncating the potential on the melting point may be related to the observation that the energy of any configuration is virtually independent of the truncation distance, while the evolution in time may be greatly influenced by the truncation distance. For calculations restricting the range to nearest neighbors, the nearest-neighbor peak in $g_2(r)$ is rather narrow and the zero between the first and the second shells persists to very high temperatures. In Ref. 29 this effect was almost canceled by the accidental use of a too smooth cutoff function [i.e., a too low value of α in Eq. (9)].

VII. COORDINATION

The coordination number for an atom may be defined as the number of atoms in the first coordination shell. At low temperature this is a well defined concept. At low temperature layer number 1 has a coordination number of 7 and is less stable than the bulk by about 500 meV. Layer number 2 has a coordination number of 11; it is less stable than bulk by about 100 meV.

While at higher temperatures it is obvious from Fig. 9 that the number of neighbors in each shell is not well defined as g_{xy} is not zero between the shells. It is possible to extend the definition of the coordination number to higher temperatures by *defining* the coordination number n_c as

$$n_c = \sum_{j \neq i} \theta(r_{cn} - r_{ij}), \tag{31}$$

where $\theta(r)$ is a stepfunction

$$\theta(r) = \begin{cases} 0 & \text{for } r \leqslant 0 \\ 1 & \text{for } r > 0 \end{cases}, \tag{32}$$

and $g_2(r_{cn})$ is the minimum of $g_2(r)$ between the first and second shells. As $g_{xy}(r)$ has a minimum but no zero between the first and second + third shell, the coordination number will depend somewhat on the actual value of r_c.

Figure 11 shows the calculated coordination numbers for calculated from the definition in Eq. (31). While the formation of vacancies in the outer layers will decrease the coordination number for the remaining atoms, the change in coordination number for the outer layers is dominated by the increase in coordination from the adatoms. For the deeper layers the coordination number decreases with temperature due to the thermal formation of vacancies and due to the presence of large amplitude phonons.

At higher temperatures when the radial distribution function no longer has a zero point between the first and second + third shell, neither the instantaneous nor the average number of atoms in the first shell has to be integer. At low temperature the distribution of coordination numbers for the dynamic atoms would be a discrete distribution, 32 atoms would have 7 neighbors, 32 atoms would have 11 neighbors, and 320 atoms would have 12 neighbors. The average distributions found at 560, 745, and 930 K are shown in Fig. 12. Although these distributions are now continuous and noninteger coordinations are abundant, the overall structure of the distributions have some resemblance

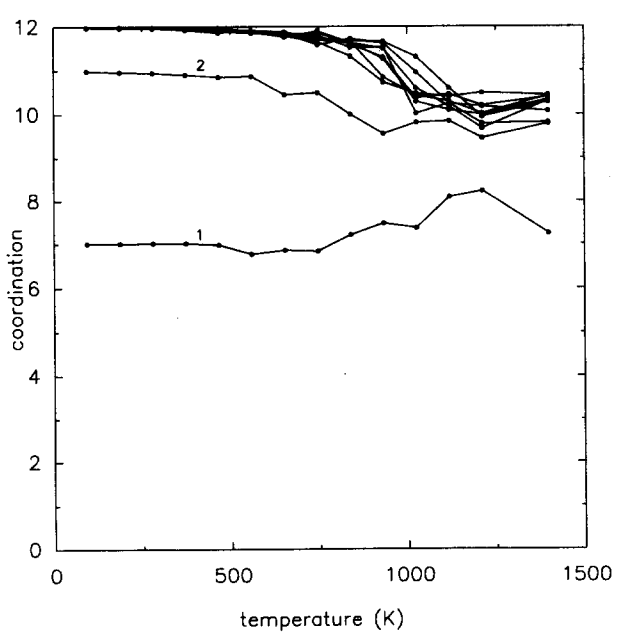

FIG. 11. Coordination number for layers as a function of temperature. At low temperature the atoms in layer number 1 have 7 nearest neighbors, the atoms in layer number 2 have 11 nearest neighbors and the atoms in deeper layers have 12 nearest neighbors. Coordination numbers at higher temperature have been calculated from the simulations by use of Eq. (31).

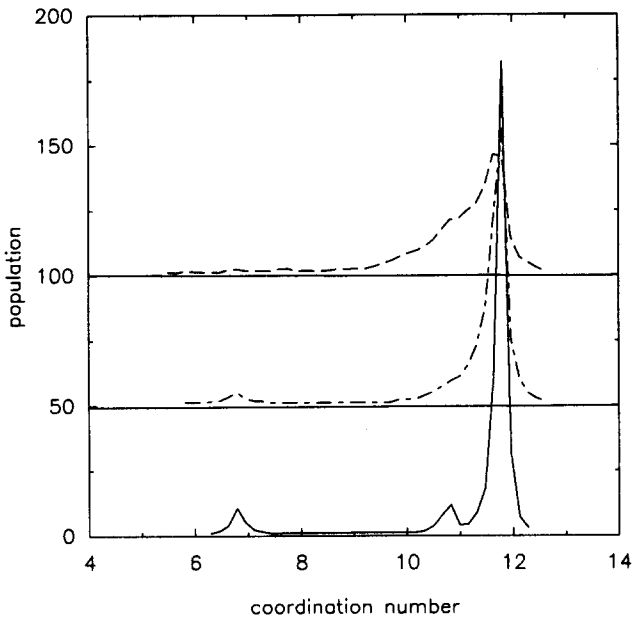

FIG. 12. Density of coordination numbers at 560 (lower), 745, and 930 K (upper). The figures have been displaced vertically for clarity. At low temperature the system will consist of 32 atoms with 7 neighbors, 32 atoms with 11 neighbors and 320 atoms with 12 neighbors. Only the distribution at 560 K has some resemblance to the low-temperature distribution. The thermal changes in the coordination number consist of a broadening in the distribution towards lower coordination numbers.

to the low temperature distribution. It is apparent from Fig. 12 that the thermally induced changes in coordination consist almost exclusively in a *decrease* of the number of neighbors.

The coordination number n_c as defined by Eq. (31) is essentially the *effective coordination number* of the Glue model[43] for bonding in metallic systems. The existence of a simple relation between n_c and the energy is essential for this model.

At low temperature when atoms are near their perfect lattice positions, a simple relation exists between energy and coordination number in the effective medium theory:

$$\begin{aligned}
&\sigma_1 = n_c \exp(-\eta_2 \beta s_0), \\
&\sigma_2 = n_c \exp(-\eta s_0), \\
&\bar{n} = n_0 \left(\frac{n_c}{12}\right)^{\eta/\beta\eta_2}, \\
&n_{\text{fcc}} = n_0 \frac{n_c}{12}, \\
&E = E_0 + E_2\left[\left(\frac{n_c}{12}\right)^{\eta/\beta\eta_2} - 1\right]^2 \\
&\quad + E_3\left[\left(\frac{n_c}{12}\right)^{\eta/\beta\eta_2} - 1\right]^3 \\
&\quad + \alpha n_0\left[\left(\frac{n_c}{12}\right)^{\eta/\beta\eta_2} - \frac{n_c}{12}\right].
\end{aligned} \tag{33}$$

During the simulation one might collect observations of the energy and the coordination number for the individual atoms. The result of such a procedure is shown in Fig. 13. Eq. (33) does not include the kinetic contributions to the

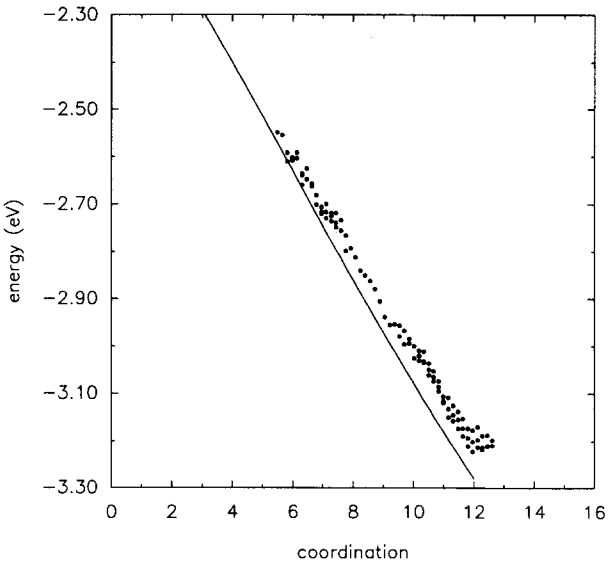

FIG. 13. Energy of an atom plotted versus the coordination number of the atom for simulations at 560, 745, and 930 K. The coordination number is calculated from Eq. (31). The energy is the total energy minus $\frac{3}{2}k_BT$ contributed by the kinetic energy. The solid curve is the energy calculated from Eq. (33).

total energy. For this reason the energy plotted in Fig. 13 has been corrected by $\frac{3}{2}k_BT$.

For the simulations at 560 and 745 K, no observations were made of coordination numbers in the range 7 to 10. However, using Eq. (33) with the simple correction for the kinetic contribution to the total energy at finite temperature seems to account fairly well for the observed data. However, a minor systematic deviation is conspicuous in Fig. (13). While C_v for real materials remain close to the harmonic value of $3k_BT$, the simulations have been performed at constant pressure, $p = 0$, and better agreement would have been found by correcting the results of the simulations using the somewhat higher value of C_p,

$$C_p = C_v + \frac{T\alpha^2 V}{\kappa}, \tag{34}$$

where α is the volume expansion coefficient, κ is the isothermal compressibility, T is the temperature, and V is the volume.

While the orientation of the surface relative to the crystal lattice determines the distribution of coordination numbers in the absence of reconstructions and the details of this distribution at high temperatures appear difficult to calculate without reference to simulations, a simple relation between the energy of the atom and the number of neighbors exists both at low and high temperature. The observation that this correlation between the energy and the coordination number holds also in rather disordered situations may indicate that at least for the situations treated here the macroscopic manifestations of the melting transitions, such as the loss of long range order and latent heat, are reflected in the single particle properties as a decrease in the coordination number.[44] It is clear from the real-space picture in Fig. 4, that the system at high temperature does not look like a well ordered lattice with some vacancies, even if the average coordination number closely parallels the thermal expansion of the system.

VIII. STRUCTURE FACTOR FOR LAYERS

As an example of a property which can be calculated but not measured, we have determined the low index structure factors $|S|^2$ for individual layers

$$S_l = \left\langle \sum_i \exp(i\mathbf{g}\cdot\mathbf{r}_i) \right\rangle, \tag{35}$$

where the averaging is made over the positions $\mathbf{r}$ of all atoms in layer number l for a lattice with lattice constants a_x,a_y, and a_z. $|S|$ may be nonzero for any wave vector $\mathbf{g}$ such that

$$\mathbf{g} = \left(\frac{2\pi n_x}{a_x}, \frac{2\pi n_y}{a_x} \right). \tag{36}$$

In the following we will label the structure factors by the integers n_x and n_y.

Figure 14 shows $|S_{(0,2)}|$ for layers 1 through 10. For all of the structure factors $|S_{(1,0)}|^2$,$|S_{(0,1)}|^2$,$|S_{(1,1)}|^2$,$|S_{(2,0)}|^2$, and $|S_{(0,2)}|^2$, we find that the structure factor for a layer decreases with temperature and that the structure factor at a given temperature increases with the layer number.

The bump in the structure factor near 570 K was first observed at 18 ps. This feature is observed in all the structure factors for the surface region and extends about six layers into the surface. This feature is apparently also observed in the density of defects, but not in the energy. The first observation of the feature coincided with the first observation of an adatom–vacancy pair. We cannot exclude the possibility that this feature is caused by some unlikely event in either the 570 or 660 K calculations, and that the bump would not develop if the calculations were restarted. However, the persistence of the bump for 50 ps could indicate that it is an

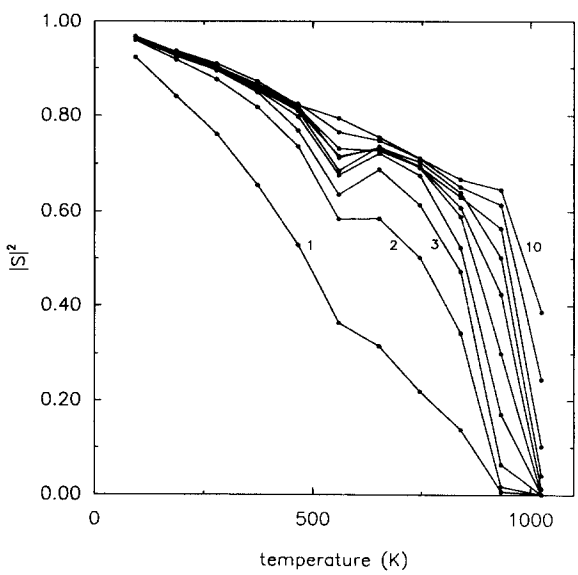

FIG. 14. The structure factor $|S_{(0,2)}|^2$ for layers 1 through 10 vs temperature. The structure factor at constant temperature is an increasing function of the layer number while the structure factor for a given layer is a decreasing function of temperature.

equilibrium phenomenon. We have checked the results presented here by a few simulations using 2048 atoms (128 atoms per layer) rather than 512 atoms (32 per layer). In this larger system we do not observe the bump in the structure factor.

In an infinite system the equilibrium concentration of defects is a smooth function of temperature. However, in the small system one atom is 3% of a monolayer and the migration of the first atom to the adlayer might lead to the release of a considerable amount of local stress. This might then be observed in the structure factor since $|S|^2$ is sensitive to strain, while the energy of the stress field might be too small to cause an anomaly in the energy. The stress at the point when the first atom migrates to the adlayer will be much smaller for the larger system.

Figure 15 shows the structure factor for layer number 1 for 5 different wave vectors. For all layers we find that the structure factor increases through the sequence

$$|S_{(2,0)}|^2 < |S_{(0,2)}|^2, |S_{(1,1)}|^2 < |S_{(1,0)}|^2, |S_{(0,1)}|^2. \quad (37)$$

At low temperature the decrease in the structure factors is caused by essentially harmonic vibrations. This may be treated quantitatively in a Debye model,[45] where

$$\ln|S|^2 = \frac{3\hbar|\mathbf{g}|^2 T}{m k_B \theta_D^2}. \quad (38)$$

The dependence of $|S|^2$ on $|\mathbf{g}|^2$ in the debye model explains the sequence of structure factors, Eq. (37).

The Debye temperature θ_D has been determined by a least squares fit to the calculated structure factors below 500 K. The results are shown in Fig. 16. For the surface we find a somewhat lower Debye temperature ($\theta_D \sim 250$ K) than for the deeper layers ($\theta_D \sim 320$ K). The calculated Debye temperature for the deeper layers is somewhat lower than the experimental value for the bulk $\theta_D = 403$ K.[46] Even if the Debye temperature in the limit $T \to 0$ may readily be calculated from the force constant for the lattice, the level of agreement between the calculated and experimental Debye temperature cannot be used to evaluate the quality of the phonon spectrum predicted by the potential. At sufficiently high temperature the Debye model will fail. This is apparent in the experimental Debye temperature determined by diffraction. The measured θ_D decreases with the temperature, T_e, of the experiment, from $\theta_D \sim 400$ K at $T_e = 0$ K, to $\theta_D \sim 380$ K at $T_e = 300$ K.[47-49] We have chosen to fit θ_D to temperatures up to 500 K. This is a temperature close to the limit of validity of the Debye model. A choice of a lower cutoff temperature for the determination of θ_D might improve the calculated Debye temperature physically, but would decrease the statistical significance of the result.

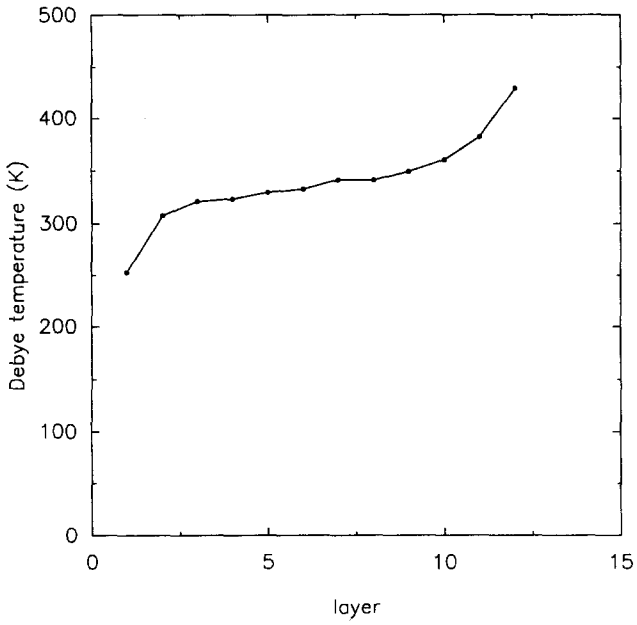

FIG. 16. Debye temperature calculated from $|S_{(1,0)}|^2$, $|S_{(0,1)}|^2$, $|S_{(1,1)}|^2$, $|S_{(2,0)}|^2$, $|S_{(0,2)}|^2$, at temperatures below 500 K.

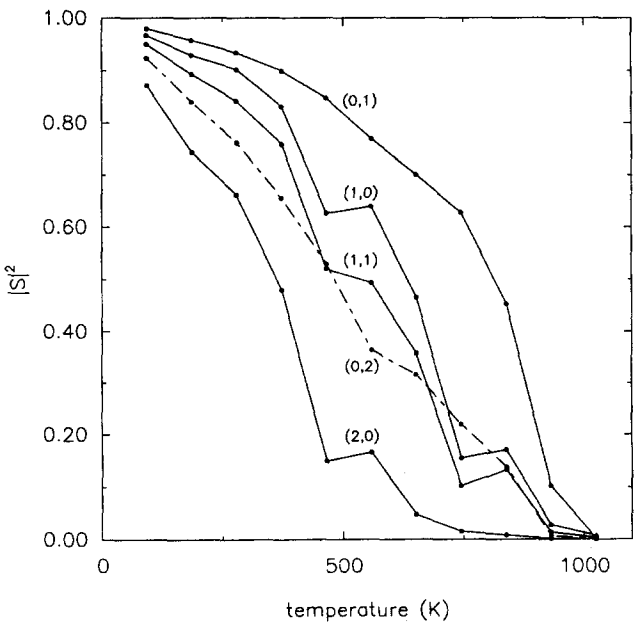

FIG. 15. Structure factors $|S_{(1,0)}|^2$, $|S_{(0,1)}|^2$, $|S_{(1,1)}|^2$, $|S_{(2,0)}|^2$, $|S_{(0,2)}|^2$ for layer number 1.

Close to the static substrate the Debye temperature is higher, as the atoms near the static substrate have small vibrational amplitudes, even if the average kinetic energy of the atoms near the static substrate is equal to the average kinetic energy of dynamic atoms in the system as a whole. The variations in Debye temperature may be interpreted as a softening of the lattice at the surface and a hardening of the lattice near the static substrate.

The transition from the infinite Debye temperature of the static atoms to that of the bulk and from the Debye temperature of the bulk to that of the surface appears to take place over 3–4 layers. The thicknesses of these two transition layers are thus close to the thickness of the solid–liquid interface.[2,4] However, Fig. 16 displays a small slope in the region between the surface and the bulk region. If this slope is significant, we cannot on the basis of the present series of simulations exclude that the thickness of the transition regions is larger than 3–4 layers.

IX. AVERAGED STRUCTURE FACTOR

From the structure factors for the layers we may calculate an average structure factor using a penetration depth λ:

$$S = \frac{\langle S_l \exp(z_l/\lambda)\rangle}{\langle \exp(z_l/\lambda)\rangle}. \quad (39)$$

For radiation with an effective penetration depth λ undergoing kinematic diffraction, the averaged structure factor will equal the normalized intensity of scattered radiation. In this interpretation **g** is the momentum transfer vector and the intensity should be normalized by the intensity at zero temperature. It is important that we calculate the averaged structure factor from $\langle S_l \exp(-z/\lambda)\rangle$ and not from $\langle |S_l|^2 \exp(-z/\lambda)\rangle$, as these two averages have different properties and are numerically quite different at high temperature.

In a LEED experiment, the electron undergoes multiple scattering. This causes a number of differences compared to the picture obtained in the kinematic scattering approximation. In the kinematic scattering approximation the (1,0) and (0,1) peaks are bulk forbidden. For multiple scattering, calculations[50] show that this selection rule no longer holds. In the calculations of the average structure factors we will not consider the (1,0) and (0,1) peaks in any detail as the results for these peaks depend sensitively on the choice of penetration depth.

By application of the kinematic scattering approximation, we will not get the dependence of the spot intensity on $|\mathbf{g}|^2$ right. However, in the kinematic scattering approximation the symmetry[51] will be correct and we will obtain a good approximation for the dependence of the intensity on temperature.[52] The argument for the correct prediction of the temperature dependence is that the electron undergoes a large number of small angle scatterings and a single backscattering, the temperature dependence of the spot intensity is, by and large, determined by this *single* backscattering event.

Figure 17 shows the averaged structure factor as a function of the penetration. If the penetration is one layer or more, we find a monotonic dependence on the penetration. However, in the limit of very short penetration we do not always find such a monotonic relationship. A closer investigation reveals that this phenomenon is caused by destructive interference between the contribution from the adatoms and the contribution from the surface layers. The experimental relevance of this observation is not obvious, presumably the diffraction spots would be extremely weak if the mean free path of the electrons is less than one atomic spacing. Theoretically this observation is more interesting, since it means that the extensive relaxations around the adatoms cause the adatoms to behave somewhat like an incommensurate overlayer.

The mean free path is approximately 7 Å at 50–100 eV,[53] corresponding to a penetration depth of 3.5 Å or 2.5 interlayer spacings. For the (1,1), (2,0), and (0,2) peaks, the averaged structure factor does not depend sensitively on the penetration depth. In the calculations of the averaged structure factors we have used a penetration depth of 2.5 interlayer spacings.

From Eq. (38) and the averaged structure factors in Fig. 18 one may calculate a Debye temperature. We find that $\theta_D = 250$ K. The closeness of this value to that for layer 1 is caused by the balance of the contributions from the adatoms and from the second layer.

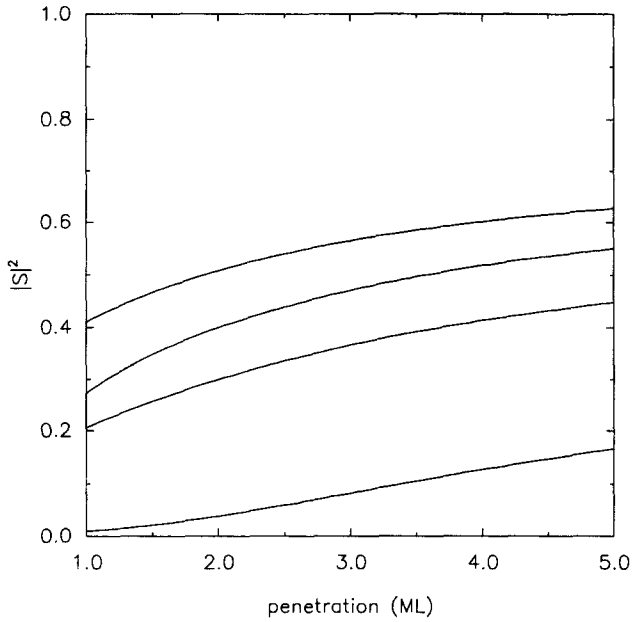

FIG. 17. The averaged structure factor for the $|S_{02}|^2$ peak at four different temperatures in the range 500 to 1000 K. The penetration used in the averaging is measured in units of monolayers. The penetration in a LEED experiment is approximately $\lambda = 2.5$ ML. The shown data are typical and serve to illustrate that the averaged structure factor does not depend sensitively on λ near $\lambda = 2.5$ ML. As explained in the text, the situation is more complicated for $\lambda < 1$ ML.

X. CORRECTION OF $|S|^2$ FOR VIBRATIONS

If one were to use the structure factor $|S|^2$ as an order parameter, this order parameter would have the awkward

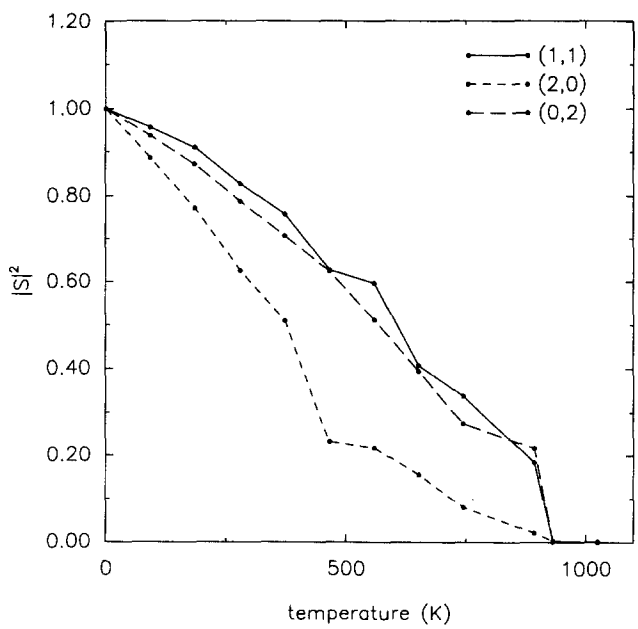

FIG. 18. Averaged structure factor for the bulk allowed (1,1), (2,0), and (0,2) peaks as a function of temperature. While $|S_{(1,1)}|^2$ and $|S_{(0,2)}|^2$ have comparable values, $|S_{(2,0)}|^2$ is lower.

feature that purely harmonic vibration would cause $|S|^2$ to drop below unity. For this choice of order parameter, purely harmonic vibration would have to be considered as a part of the disorder. We may use the calculated Debye temperature to correct this problem by defining another order parameter, $|S'|^2$

$$\ln|S|^2 = \frac{3\hbar g^2 T}{m k_B \theta_D^2} + \ln|S'|^2. \tag{40}$$

For a perfect lattice and for a lattice undergoing harmonic vibrations $|S'|^2$ is unity.

The calculated $|S'|^2$ is shown in Fig. 19. It appears that this choice of order parameter leads us to conclude that the loss of order in the lattice is anisotropic,[13,14] as $|S'_{(2,0)}|^2$ drops significantly faster than $|S'_{(1,1)}|^2$ or $|S'_{(0,2)}|^2$. The same conclusion is reached if we consider $|S'|^2$ calculated for individual layers. The apparent anisotropy of the onset of the melting has been found from LEED intensity measurements for Pb(110).[13,14] If the conclusion based on the order parameter $|S'|^2$ is taken at face value, we are lead to the conclusion that the disorder close to the melting point is strongest *along* the close-packed rows of the (110) surface. It may be useful to investigate further the properties of $|S'|^2$.

If $|S|^2$ is used as an order parameter, vibrations will be considered as a part of the disorder. If $|S'|^2$ is used as an order parameter, *harmonic* vibrations will no longer contribute to the disorder. By comparing Eq. (40) to the results for the Debye–Waller factor for anharmonic lattices[54] it is found that anharmonic vibrations will cause $|S'|^2$ to drop below unity and, further, that this drop depends on $|\mathbf{g}|^2$. This may be illustrated by the following toy model.

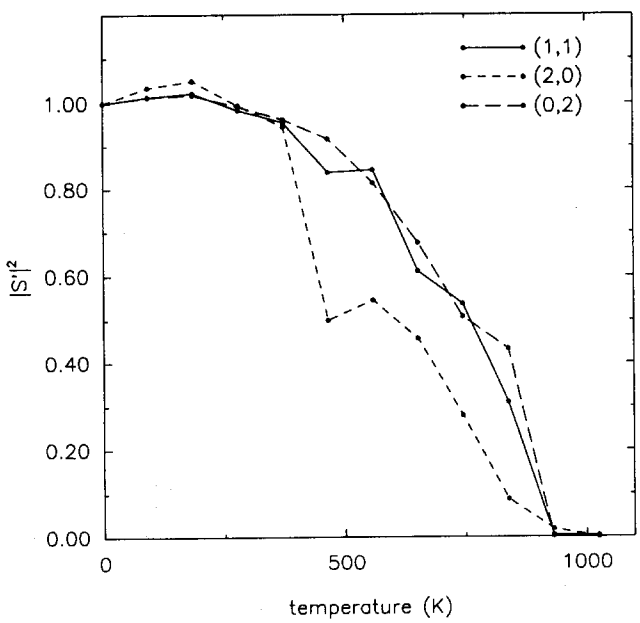

FIG. 19. The order parameter $|S'|^2$ calculated by correcting the exponentially averaged structure factor in Fig. 18 using the Debye temperature, Eq. (39). As in Fig. 18 we find that while $|S'_{(1,1)}|^2$ and $|S'_{(0,2)}|^2$ have comparable values, $|S'_{(2,0)}|^2$ is lower.

Assume an Einstein model for the bonds

$$V = \tfrac{1}{2}\kappa(l - l_0)^2, \tag{41}$$

where κ is the spring constant, $\kappa = \kappa_0$ at $T = 0$, l is the actual bond length, and l_0 is the equilibrium bond length. Further assume a Grüneisen model for the anharmonicity:

$$\frac{\partial \omega}{\partial T} = \gamma \omega \alpha, \tag{42}$$

where ω is the resonance angular velocity, $\kappa = m\omega^2$, γ is the Grüneisen parameter, and α is the volume expansion coefficient. In this model the partition function Z and the thermally averaged structure factor $|S|^2$ may easily be found:

$$Z = \int \exp\left[-\frac{\kappa(l - l_0)^2}{2k_B T} \right] dl \tag{43}$$

$$S = Z^{-1} \int \exp(igl) \exp\left[-\frac{\kappa(l - l_0)^2}{2k_B T} \right] dl. \tag{44}$$

By expansion to second order in T,

$$\ln|S|^2 = -\frac{g^2 k_B T}{\kappa_0} - g^2 k_B \times (12\gamma\alpha\kappa_0 + g^2 k_B) T^2 + o(T^3), \tag{45}$$

we find that the leading term in both $\ln|S|^2$

$$\ln|S|^2 = -\frac{g^2 k_B T}{\kappa_0} \tag{46}$$

and in $\ln|S'|^2$

$$\ln|S'|^2 = -g^2 k_B 12\gamma\alpha\kappa_0 T^2 \tag{47}$$

are proportional to g^2. This suggests that one may analyze the order parameter $|S''|^2$ defined by

$$\ln|S|^2 = g^2 \ln|S''|^2. \tag{48}$$

Vibrations will cause this order parameter to drop below unity and vibrations will contribute to the disorder measured by $|S''|^2$. However, the leading terms in $|S''|^2$ are independent of $|\mathbf{g}|^2$. In other words $|S''|^2$ is independent of the momentum transfer, $\Delta\mathbf{p} = \hbar\mathbf{g}$, made in the *observation* of the disorder by a diffraction technique.

Figure 20 shows the order parameter $|S''|^2$ calculated from the averaged structure factor $|S|^2$ in Fig. 17. The coincidence of $|S''_{(1,1)}|^2$, $|S''_{(2,0)}|^2$ and $|S''_{(0,2)}|^2$ strongly suggest that the anisotropy observed by using $|S|^2$ (Fig. 17) or $|S'|^2$ (Fig. 19) as order parameters may be accounted for by the dependence of $|S|^2$ and $|S'|^2$ on $|\mathbf{g}|^2$. In other words the anisotropy is not in the atomic structure itself but enters through the anisotropy in the observation. As the unit cell of a fcc (110) surface is rectangular, the Bragg condition implies different values for $|\mathbf{g}|^2$ along x and y.

XI. CONCLUSIONS

To summarize, we have studied the premelting of Al(110) by molecular dynamics simulations. The potential used in the simulations is the potential for Al derived from effective medium theory. From the derivation and from the previous applications of this potential we expect that it should give a good description of metallic systems, while the computational effort remains moderate.

The setup used consisted of 512 atoms with periodic

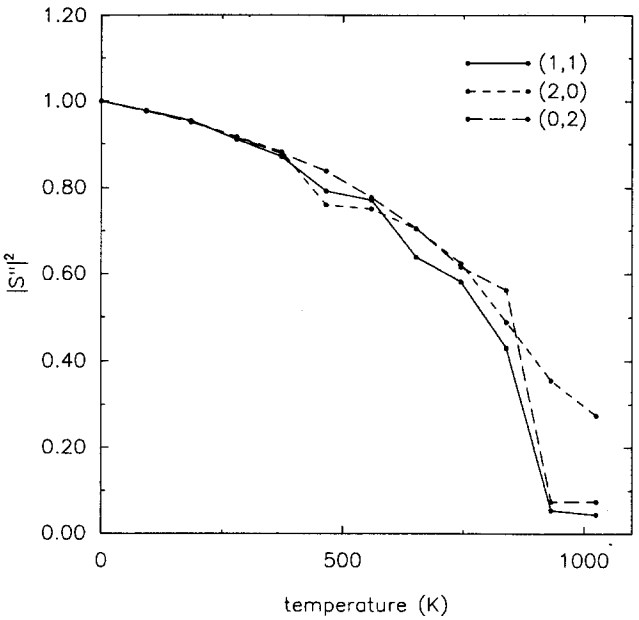

FIG. 20. The order parameter $|S''|^2$ calculated by correcting the averaged structure factor in Fig. 18 by the length of the wave vector **g**, Eq. (48).

boundary conditions in X and Y and four layers of static atoms. This setup is suitable for the study of the onset of disorder. Except for the details of the onset of the disorder of the surface region, we have found no finite-size effects by repetition of some of the simulations for a larger system.

At high temperature we find evidence for premelting in the form of a progressive disordering of the surface region. This disordering is mediated by the formation of adatom–vacancy pairs. The correlation of the onset of the disorder with the formation of adatom–vacancy pairs is not inconsistent with Tammanns hypothesis on the importance of surfaces for bulk melting.

The surface energy has been calculated as the difference in total energy between the semiinfinite crystal and the bulk crystal. Close to the melting point, the surface energy increases steeply due to the disordering of the surface region. At these conditions several layers contribute to the surface energy.

The concept of coordination numbers is generalized to higher temperatures based on an investigation of the radial distribution function. The coordination number for atoms has a simple relation to the energy in the effective medium theory. From the data of the simulations we find that after allowance for the kinetic contribution to the total energy this correlation remains at high temperatures and for disordered structures. This suggests that, at least for the situations considered here, the thermodynamics of the disorder is reflected in the single particle properties by a decrease in the coordination number.

Some structure factors have been calculated for the layers as well as averaged data, using an effective penetration depth relevant for comparison with LEED experiments. From the averaged structure factors we have calculated two other order parameters. The order parameter $|S'|^2$ is $|S|^2$ corrected for harmonic vibrations, Eq. (40). If $|S|^2$ or $|S'|^2$ are used as measures of the order of the surface region, the onset of the disorder appears to be anisotropic. Inspired by a toy model we have calculated the order parameter $|S''|^2$ by correcting $|S|^2$ for the dependence on the length of the wave vector, Eq. (48). If $|S''|^2$ is used as a measure of the order of the surface region, the onset of the disordering appears isotropic. This strongly suggests that the apparent anisotropy in the disordering of the surface region is caused by the *detection* of the disorder either experimentally by a diffraction or numerically by Fourier transformation.

ACKNOWLEDGMENTS

The discussions I have had with Jens K. Nørskov, Uzi Landman, and Arnoud Denier van der Gon in the course of this work are gratefully appreciated. This work has been financed by the Danish Research Council under FTU Contract No. 5.17.1.1.11.

[1] J. A. Barker and D. Henderson, Rev. Mod. Phys. **48**, 587 (1976).
[2] W. A. Curtin and N. W. Ashcroft, Phys. Rev. Lett. **56**, 2775 (1986).
[3] S. W. Koch, *Dynamics of first-order phase transitions in equilibrium and non-equilibrium systems* Lecture Notes in Physics Vol. 207, (1984).
[4] W. A. Curtin, Phys. Rev. Lett. **59**, 1228 (1987).
[5] D. P. Woodruff, *The Solid–Liquid Interface* (Cambridge University, Cambridge, 1973).
[6] J. W. M. Frenken and J. F. van der Veen, Phys. Rev. Lett. **54**, 134 (1985).
[7] J. W. M. Frenken, P. M. J. Marée, and J. F. van der Veen, Phys. Rev. B **34**, 7506 (1986).
[8] B. Pluis, A. W. Denier van der Gon, J. W. M. Frenken, and J. F. van der Veen, Phys. Rev. Lett. **59**, 2678 (1987).
[9] B. Pluis, J. W. M. Frenken, and J. F. van der Veen, Phys. Scr. T **19**, 382 (1987).
[10] J. F. van der Veen, B. Pluis, and A. W. Denier van der Gon, Chem. Phys. Solid Surf. **7**, 455 (1988).
[11] J. W. M. Frenken, J. P. Toennies, and Ch. Wöll, Phys. Rev. Lett. **60**, 1727 (1988).
[12] P. von Blankenhagen, W. Schommers, and V. Vogele, J. Vac. Sci. Technol. A **5**, 649 (1987).
[13] K. C. Prince, U. Breuer, and H. P. Bonzel, Phys. Rev. Lett. **60**, 1146 (1988).
[14] R. Lipowsky, U. Breuer, K. C. Prince, and H. P. Bonzel, Phys. Rev. Lett. **62**, 913 (1989).
[15] P. H. Fuoss, L. J. Norton, and S. Brennan, Phys. Rev. Lett. **60**, 2046 (1988).
[16] G. Jezequel, P. Thiry, G. Rossi, K. Hricovini, and Y. Petroff, Surf. Sci. **189/190**, 605 (1987).
[17] E. T. Chen, R. N. Barnett, and U. Landman, Phys. Rev. B **40**, 924 (1989).
[18] R. Lipowsky, Phys. Rev. Lett. **49**, 1575 (1982).
[19] H. Nakanishi and M. E. Fisher, Phys. Rev. Lett. **49**, 1565 (1982).
[20] R. Lipowsky and W. Speth, Phys. Rev. B **28**, 2983 (1983).
[21] R. Lipowsky, Z. Phys. B **55**, 345 (1984).
[22] R. Lipowsky, Ferroelectrics **73**, 69 (1987).
[23] J. M. Ziman, *Models of Disorder* (Cambridge University, Cambridge, 1979).
[24] J. Q. Broughton and G. H. Gilmer, J. Chem. Phys. **79**, 5095 (1983).
[25] J. Q. Broughton and G. H. Gilmer, J. Chem. Phys. **79**, 5105 (1983).
[26] J. Q. Broughton and G. H. Gilmer, J. Chem. Phys. **79**, 5119 (1983).
[27] V. Rosato, G. Ciccotti, and V. Pontikis, Phys. Rev. B **33**, 1860 (1986).
[28] V. Pontikis and P. Sindzingre, Phys. Scr. T **19**, 375 (1987).
[29] P. Stoltze, J. K. Nørskov, and U. Landman, Phys. Rev. Lett. **61**, 440 (1988).
[30] P. Stoltze, J. K. Nørskov, and U. Landman, Surf. Sci. **220**, L693 (1989).
[31] K. W. Jacobsen, J. K. Nørskov, and M. J. Puska, Phys. Rev. B **35**, 7423 (1987).
[32] K. W. Jacobsen, Comments Condens. Matter. Phys. **14**, 129 (1988).
[33] P. Stoltze, K. W. Jacobsen, and J. K. Nørskov, Phys. Rev. B **36**, 5035 (1987).
[34] J. K. Nørskov and K. W. Jacobsen, in *The Structure of Surfaces II*, edited

by J. F. van der Veen and M. A. van Hove, Springer Series in Surf. Sci. Vol II (Springer, New York, 1978), p. 118.
[35] K. W. Jacobsen and J. K. Nørskov, Phys. Rev. Lett. **59**, 2764 (1987).
[36] K. W. Jacobsen and J. K. Nørskov, Phys. Rev. Lett. **60**, 2496 (1988).
[37] J. K. Nørskov, J. Chem. Phys. **90**, 7461 (1989).
[38] O. B. Christensen, P. Ditlevsen, K. W. Jacobsen, P. Stoltze, O. H. Nielsen, and J. K. Nørskov, Phys. Rev. B **40**, 1993 (1989).
[39] D. W. Heerman, *Computer Simulation Methods in Theoretical Physics* (Springer, New York, 1986).
[40] Y. Imry, Phys. Rev. B **21**, 2042 (1980).
[41] R. Hultgren, P. D. Desai, D. T. Hawkins, M. Gleiser, K. K. Kelley, and D. D. Wagman, *Selected Values of the Thermodynamic Properties of the Elements* (American Society for the Metals, Metals Park, Ohio, 1973).
[42] F. F. Abraham, Adv. Phys. **35**, 1 (1986).
[43] F. Ercolessi, E. Tosatti, M. Parinello, Phys. Rev. Lett. **57**, 719 (1986).
[44] N. H. March, Phys. Chem. Liq. **17**, 1 (1987).
[45] J. M. Ziman, *The Principles of the Theory of Solids* (Cambridge University, Cambridge, 1965).
[46] K. A. Gschneidener, Jr., Solid Stat. Phys. **16**, 275 (1964).
[47] P. A. Flinn and M. McManus, Phys. Rev. **132**, 2458 (1963).
[48] R. M. Nicklow and R. A. Young, Phys. Rev. **152**, 591 (1966).
[49] G. Gilat and R. M. Nicklow, Phys. Rev. **143**, 487 (1966).
[50] J. R. Noonan and H. L. Davies, Phys. Rev. B **29**, 4349 (1984).
[51] M. Henzler, in *Electron Spectroscopy for Surface Analysis*, edited by H. Ibach, Topics in Current Physics, Vol. 4 (Springer, Berlin, 1977).
[52] D. P. Woodruff and T. A. Delchar, *Modern Surface Science Techniques* (Cambridge University, Cambridge, 1986).
[53] A. Zangwill, *Physics at Surfaces* (Cambridge University, Cambridge 1988).
[54] A. A. Maradudin and P. A. Flinn, Phys. Rev. **129**, 2529 (1963).